Desalination and Water Treatment
www.deswater.com

doi: 10.5004/dwt.2019.23558

143 (2019) 165–177
March

CFD analysis of the tube bundle orientation impact on the thermal losses and vapor uniformity within the MED desalination plant

Abdelnasser Mabrouk[a,b,*], Ahmed Abotaleb[c]

[a]*Qatar Environment & Energy Research institute, Hamad Bin Khalifa University, Qatar Foundation, P.O. Box 34110 Doha, Qatar, email: aaboukhlewa@hbku.edu.qa*
[b]*College of Science and Engineering, Hamad Bin Khalifa University, Qatar Foundation, Qatar*
[c]*Qatar Environment & Energy Research institute, Hamad Bin Khalifa University, Qatar Foundation, Qatar, email: aabotaleb@hbku.edu.qa*

Received 5 July 2018; Accepted 1 December 2018

ABSTRACT

Thermal desalination still considered as a reliable technology, where the seawater characteristic is challenging in terms of high salinity, elevated temperature and high impurity level especially in the Gulf seawater case. Multi-effect distillation (MED) is an efficient thermal process for the commercial and large-scale desalination plants. Even though, minimization of the thermal losses within the evaporator is a matter of interest to improve the MED process. This work presents a computational fluid dynamic (CFD) simulation of vapor route for two conventional MED configurations named as long tube (MED-LT) and cross tube (MED-CT), respectively. The thermal losses and vapor uniformity are calculated at several vapor box lengths and process recovery ratios. An MED evaporator of 25 m^3/d is considered for the CFD computational domain and conducted by COMSOL multiphysics. The CFD results show that compared by MED-LT configuration, the MED-CT configuration creates less uniform vapor flow at the tube sheet which indicates that some tubes will be admitted by amount of vapor higher than the designed, and accordingly will become overheated and lead to the scale deposition on the tube surface. The tube bundle losses represent 90% of the total losses while the rest is encountered in the demister and vapor box. This indicates that minimizing the thermal losses in the tube bundle is more effective and recommended for future work. The footprint of the MED-LT configuration is 25% lower than that the MED-CT configuration. It can be concluded that the MED-LT configuration is superior in terms of better vapor uniformity for reliable operation and lower foot print.

Keywords: Desalination; MED; Thermal losses; CFD; Vapor route; Vapor box

1. Introduction

Thermal desalination still considered as a reliable technology, where the seawater characteristic is challenging in terms of high salinity, elevated temperature and high impurity level especially Gulf seawater case. Thermal desalination, including multi-stage flash (MSF) and multi-effect distillation (MED) technologies dominate the desalination industry in the Gulf Cooperation Council (GCC) countries, while, the reverse osmosis (RO) membrane technology getting a growing market due to its energy efficiency. In Qatar, the thermal desalination dominates 75% of the market, while the rest is shared by RO [1]. The harsh gulf seawater conditions (elevated temperature, high salinity, high impurity, and sometimes red tide) prefer the thermal desalination technology as a reliable solution. Among the thermal desalination technologies, the MED operates at lower specific power consumption than the MSF because of using falling film evaporation around tubes (three times of the distillate) instead of pumping a bulk flow of seawater feed (10 times of the product) [2].

* Corresponding author.

Falling film evaporator is the core technology of MED desalination process. The evaporation rate depends on the heat transfer kinetics, the tube wall surface characteristic and the falling film seawater properties. The temperature difference between the wall and the falling film is the driving force to increase the evaporation rate. However, this approach enables the nucleate boiling (bubble formation), which ruptures the film evaporation. An expression for the maximum wall temperature prior to bubble formation is developed by Mitrovic [3]. Thus, specifying the heat transfer conditions without the film rupture arising from bubble inception.

The effect of micro-bubbles within the thin film layer around horizontal tube is experimentally depicted particularly when the saturation temperature drop below 298 K. A new correlation is proposed for film evaporation coefficient [4]. The generated micro-bubble enhanced the heat transfer due to rapid increase of the bubble in the thin film layer.

The concept of film evaporation in the solar still showed an improvement by 30% compared with the conventional design bulk evaporation [5]. In which the evaporation transfer likely depends on the water layer thickness. The concept of falling film evaporation superseded the bulk evaporation and became the state of art in the MED technology for seawater technology [6]. Energy efficient MED process powered by solar linear Fresnel collector is proposed to reduce the mechanical energy equivalent from 19 to 8 kWh/m^3 [7] because of using low-quality steam at 70°C and 0.3 bar while the gain output ratio (GOR) of the system is calculated with 8. However, the thermal loss within evaporator is still a matter of interest of the present work.

Advanced desalination hybridizing a conventional MED and emerging yet low energy adsorption is numerically and experimentally investigated [8–10]. The adsorption system enabled the lower brine temperature, which allows to accommodate additional condensation evaporation effects that increases the GOR up to 40%. Moreover, significant increase in the production rate up to twofold of the conventional MED.

A definition of the performance ratio is redefined based on the exergy analysis and named as universal performance ratio [11,12], which reflects the exergy destruction within the power cycle and its effect on the steam quality allocated to desalination process. The universal performance ratio has improved by 55% [12] by using hybrid MED and adsorption cycle [11,12]. The exergy approach is not only accurately allocating the primary energy among stream of cogeneration power and desalination plant but also allocate the accurate cost of the water and electricity [13]. The fair and accurate methodology of energy and cost allocation would encourage process engineers to revisit the reliable thermal process especially in GCC area, where the seawater conditions are challenging to RO technology. Nevertheless, this work aims to evaluate the thermal losses within the conventional and existing MED desalination plant and exploit the possibility for improvement.

The vapor flow through the tube bundle of a falling film evaporator affects the MED process performance and the encountered thermal losses due to pressure drops. The generated vapor around evaporator tubes flows crossover the tubes, and intersects with falling film before sweeping from both sides of the tube bundle. At high vapor velocity region, the vapor velocity might deflect the falling film away from the next tube, which results in an incomplete wetting of the lower tubes. Lorenz et al. [14] determined the falling film angle beyond which the falling film will not wet the lower tube. Based on the tube bundle arrangement and the critical deflection angle, they developed the maximum allowable vapor crossflow velocity. Nevertheless, pressure drop (thermal losses) due to friction loss around tubes generates thermal losses, which increase the required heat transfer area to achieve the product capacity.

Analysis of the heat transfer coefficient in a square-pitch bundle arrangement for falling film evaporation, showed an increase in the heat transfer coefficient from row to row[15]. While, in the triangular-pitch bundle it decreases the heat transfer coefficient from row to row, particularly with high heat fluxes and lower flow rates [15,16].

The tube bundle arrangement has a considerable influence in the falling film pattern, the wettability criteria and the rate of the scale deposition. The uneven distribution of dripping seawater among tubes in vertical columns in a triangle pitch tube bundle arrangement is simulated and the developed model includes $CaCO_3$ scale formation and CO_2 release [17]. The simulation results showed that the flow rate of the dripping seawater on the column, based on the second row is lower than that of the first row. Consequently, the wetting rate of the tubes in the column based on the second row is less than that on the first row, which explains why the tubes based on the second row experience more $CaCO_3$ scale deposit than that on the first row [17].

In addition to that, many studies have presented process simulation (zero-dimensional mathematical modeling) of the MED process [18–26], which included empirical correlations for thermal losses occur within tube bundle, demister, and vapor box. Those equations are used to calculate the available temperature difference. Accordingly, the heat transfer area and sizing the evaporator tube bundle was calculated. The zero-dimensional models focus on the entire system design and performance. However, it does not provide sufficient information about the effect of the tube bundle orientation and the vapor route resistance within evaporator (tube bundle, demister, and vapor box).

Numerical computational fluid dynamic (CFD) analysis was conducted to investigate the effect of the velocity variations on the brine carry over factor and the demister pressure drop [27], where the trajectory of liquid droplets associated with the vapor released from tube bundle was calculated using Lagrange approach. A new baffle configuration shows a minimum brine carry over factor of 0.097, while the demister pressure drop is less than 13.4% of the original design.

Two existing MED desalination plants are shown in Figs. 1(a) and 2(a), which they are still commercially in operation [28]. The key features of the two configurations, the tube bundles are arranged with respect to the vapor route in long tube evaporator (MED-LT) and cross tube evaporator (MED-CT) as shown in Figs. 1(b) and 2(b), respectively.

Fig. 1(b) shows the top view of the long tube evaporator (MED-LT) configuration in which, the vapor box is in between two effects to transport vapor from effect to the successive effect. The generated vapor swept out from both sides of the tube bundle and passed through the horizontal demister. After demister, the vapor moves in parallel to the tube to be collected in the vapor box.

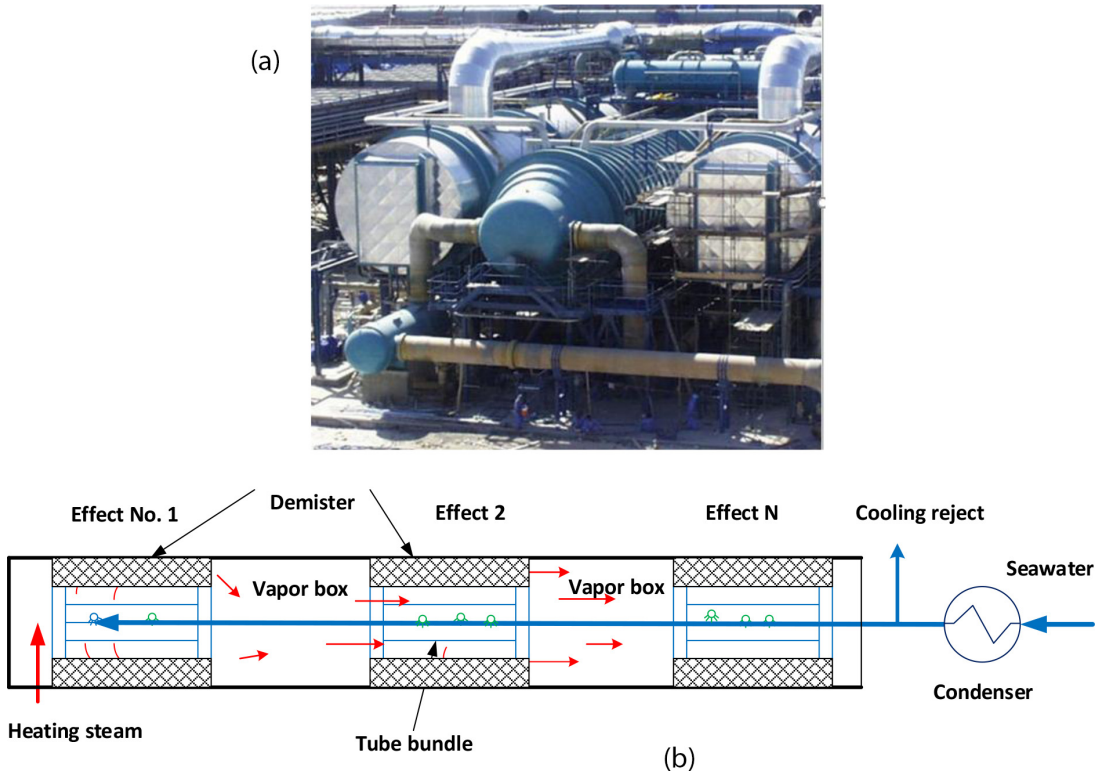

Fig. 1. (a) MED desalination plant of unit capacity (3.77 MIGD) and long tube configuration, UAE. (b) Top view of long tube evaporator (MED-LT).

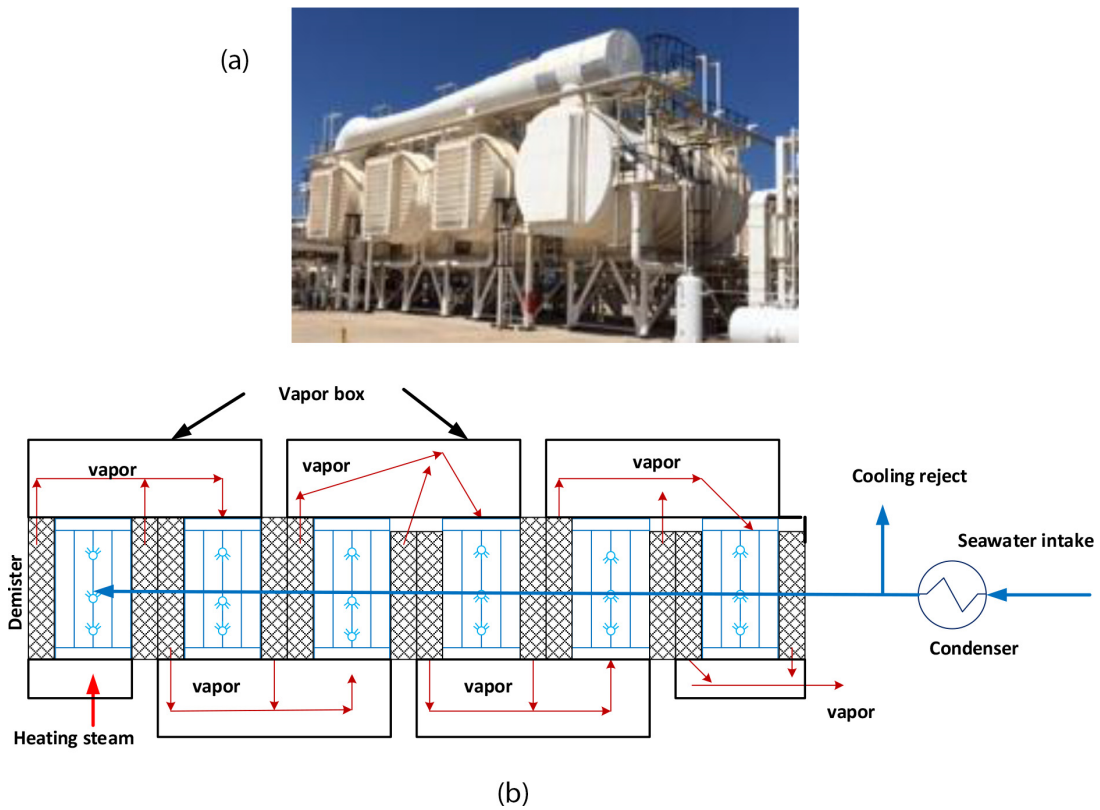

Fig. 2. (a) MED desalination plant of unit capacity (1 MIGD unit) and cross tube configuration, Qatar. (b) Top view of cross tube evaporator (MED-CT).

In the cross tube evaporator (MED-CT), the tube bundles are arranged side by side as shown in Fig. 2(b). The demister is in both sides of the tube bundle, while the vapor box is located alternatively opposite to the tube bundle. The generated vapor is also swept out from both sides of the tube bundle and passed through the horizontal demister. Then, the vapor is directed to the vapor box before induced to the next effect. Since the vapor must make a U-turn to reach the next effect, relatively higher vapor vortices would be generated in the vapor box compared with the MED-LT configuration.

In both configurations, the pressure drop occurs within the tube bundle, demister and the vapor box due to friction, separation and sudden change in the flow path, which expresses the thermal losses within the vapor route. The vapor route resistance is not only affected by the falling film pattern either columns or droplet but also affected by the friction of crossing vapor over tubes. In fact, as the vapor route becomes longer, the thermal resistance and losses get higher (for high-capacity MED). The vapor route resistance would be affected by the tube orientation, demister height and the vapor box orientation.

In case the vapor flow is not uniform at the tube sheet of the next effect, practical and technical challenges would face the evaporator performance. If, for example, some tubes are admitted by amount of vapor higher than the designed, it will become overheated. While seawater falling on the overheated surface, the scale deposition will be formed, which significantly affects the heat transfer process. On the other hand, for the tubes that are under-estimate amount of admitted vapor, the insufficient heat being released to generate vapor will affect the evaporator performance. Moreover, monitoring where the thermal losses are created and determined that the most influence design and process parameters is a matter of importance that would help to minimize it and find out solution.

To the best knowledge of the authors, there is no CFD work address the vapor uniformity and thermal losses in the entire MED evaporator. The motivation of this work is to investigate the effect of the tube bundle orientation on the vapor uniformity and thermal losses in both configuration and evaluate thermal losses in each segment in the evaporator. The aim of this work is to compare between long tube (MED-LT) and cross tube (MED-CT) configurations which have different tube orientation. Using CFD, two configurations are simulated to determine thermal losses in the tube bundle, demister, and vapor box. Nevertheless, the CFD enables to determine the vapor uniformity in the vapor box in both configurations.

2. CFD model development

2.1. Mathematical model

Steady state 2D and 3D CFD models are developed for one effect of the MED evaporator using COMSOL multiphysics v.5.2a.

The mathematical modeling approach has been developed based on the following assumptions:

- Steady state
- Weakly compressible Newtonian flow
- Demister as porous media
- The model is under vacuum pressure
- Saturated steam flow inlet to demister and vapor box at 50°C
- Fully developed inlet vapor flow

Conservation of mass:

$$\frac{\partial \rho}{\partial t} + \nabla(\rho u) = 0 \tag{1}$$

where ρ is the fluid density while u are fluid velocity t is time.

Conservation of momentum:

$$\rho\left[u\frac{\partial u}{\partial x} + v\frac{\partial u}{\partial y} + w\frac{\partial u}{\partial z}\right] = -\frac{\partial P}{\partial x} + \eta\left[\frac{\partial^2 u}{\partial x^2} + \frac{\partial^2 u}{\partial y^2} + \frac{\partial^2 u}{\partial z^2}\right] + \rho g \tag{2}$$

$$\rho\left[u\frac{\partial v}{\partial x} + v\frac{\partial v}{\partial y} + w\frac{\partial v}{\partial z}\right] = -\frac{\partial P}{\partial y} + \eta\left[\frac{\partial^2 v}{\partial x^2} + \frac{\partial^2 v}{\partial y^2} + \frac{\partial^2 v}{\partial z^2}\right] + \rho g \tag{3}$$

$$\rho\left[u\frac{\partial w}{\partial x} + v\frac{\partial w}{\partial y} + w\frac{\partial w}{\partial z}\right] = -\frac{\partial P}{\partial z} + \eta\left[\frac{\partial^2 w}{\partial x^2} + \frac{\partial^2 w}{\partial y^2} + \frac{\partial^2 w}{\partial z^2}\right] + \rho g \tag{4}$$

Transport equations for the Standard k – ε model where the turbulent kinetic energy:

$$\frac{\partial}{\partial x_j}\left(\rho k u_j\right) = \frac{\partial}{\partial x_j}\left[\left(\mu + \frac{\mu_t}{\sigma_k}\right)\frac{\partial k}{\partial x_j}\right] + \mu\frac{\partial u_i}{\partial x_j}\left[\frac{\partial u_i}{\partial x_j} + \frac{\partial u_j}{\partial x_i}\right] - \rho\varepsilon \tag{5}$$

Rate of dissipation:

$$\frac{\partial}{\partial x_j}\left(\rho\varepsilon u_k\right) = \frac{\partial}{\partial x_k}\left[\left(\mu + \frac{\mu_t}{\sigma_\varepsilon}\right)\frac{\partial \varepsilon}{\partial x_k}\right] + \frac{c_1\varepsilon}{k}\mu\frac{\partial u_i}{\partial x_j}\left(\frac{\partial u_i}{\partial x_j} + \frac{\partial u_j}{\partial x_i}\right) - c_2\rho\frac{\varepsilon^2}{k} \tag{6}$$

2.2. Model domain and boundary conditions

Fig. 3 shows 3D geometry of the MED-LT configuration with dimension in meter. Due to symmetrical geometry, it is decided to build half of the domain to save the computation time. On the other hand, Fig. 4 shows 3D geometry and domain of the MED-CT configuration. The 3D geometry is built on the full tube bundle due to the unsymmetrical vapor flow specifically in the vapor box. The computational domain consists of three zones:

- Falling film evaporation within tube Bundle: steady state two-dimensional model based on Euler-Euler laminar flow package is used to calculate the evaporation rate and vapor field around tubes and its movement to sweep out from the bundle. The two-phase pressure drop encountered vapor transportation over tubes is calculated. The physics interface considered the flow at low and moderate Reynolds number. Two sets of Navier-Stokes equations have been solved, one for each phase, to determine each

phase velocity field. The phases interchange momentum is described by a drag model. The pressure is calculated from a mixture-averaged continuity equation and the volume fraction of the dispersed phase is tracked with a transport equation. It's worth mentioning that, there are similar studies used Euler-Euler physics to model two phase evaporation [29–32].

- Vapor flow through demister: steady state two-dimensional model using Darcy's Law interface to simulate fluid flow through porous medium at low-velocity flows. Demister porosity and permeability are the main design parameters for efficient separation. The pressure gradient is the major driving force and the frictional resistance within the pores mostly influences the flow. It is well known to use Darcy's law in modeling demister/mist eliminator [27].
- Vapor flow through the vapor box: Steady state three-dimensional model using non-isothermal turbulent $k-\varepsilon$ flow package model is used to model the vapor flow in the domain above demister and the vapor box. The non-isothermal flow calculations are based on coupling the Navier–Stokes equations for conservation of momentum and the continuity equation for conservation of mass. The turbulence effects are modeled using the standard two-equation $k-\varepsilon$ model. Flow close to walls is modeled using wall functions. The standard $k-\varepsilon$ model was selected due to its robustness and the low computational time compared with other turbulence model for this specific problem [27].
- As shown in Table 1, the boundary conditions of the computational domain are presented. The heating steam

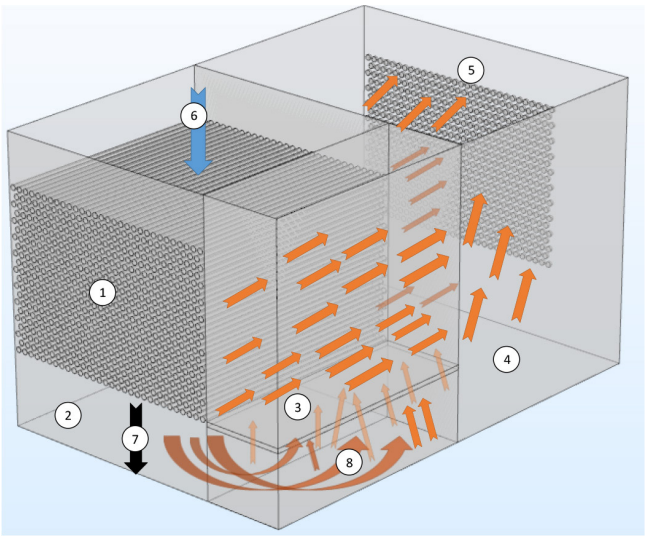

Fig. 3. 3D sketch of the CFD domain of long tube configuration: (1) tube bundle, (2) sump, (3) demister, (4) vapor box, (5) tube bundle of the second effect, (6) inlet seawater, (7) brine outlet, and (8) released vapor.

Table 1
Boundary conditions for one effect of MED evaporator

Parameter	Value
Falling film flow rate (feed seawater), m^3/h	3
Feed temperature, °C	50
Feed salinity, g/L	45
Inlet vapor temperature, °C	53
Generated vapor temperature, °C	50
Recovery ratio, %	11–33
No. of tubes	620
Tube diameter (OD), mm	25.4
Tube length, m	1
Vapor box length, m	0.25–1
Tube bundle height, m	0.7
Tube bundle width, m	2

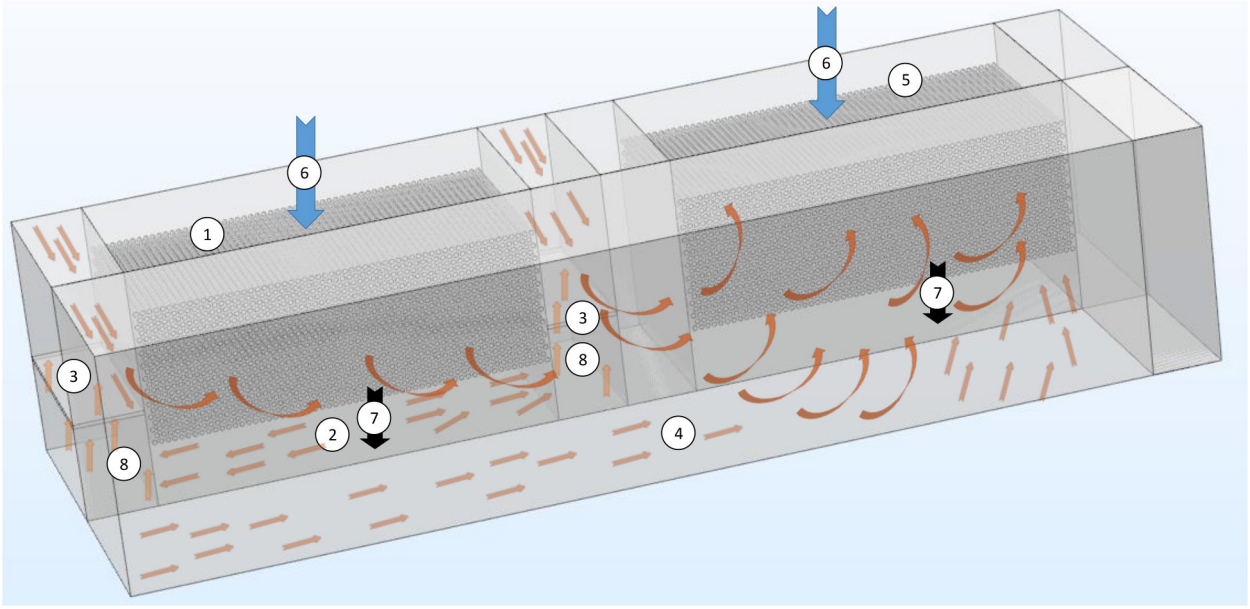

Fig. 4. 3D geometry and domain of the MED-CT configuration.

is admitted to the tube bundle at 53°C to be condensed inside the tubes and transfer the latent to the sprayed seawater falling film outside the tubes. Part of the falling film is converted as a vapor at 50°C, while the remaining brine is fallen in the brine sump at slightly higher temperature to consider the boiling point elevation. The tube bundle consists of 620 tubes arranged in a triangular tube pitch configuration. The outside tube diameter is 25.4 mm and 1 m length. Demister thickness is 20 mm. The effect of the vapor box length on the thermal losses and vapor uniformity also is investigated at different recovery ratio (the ratio between the amounts of generated vapor to the amount of seawater falling film) of 11%, 22%, and 33% to consider a wide range of vapor velocity in practical MED desalination plants. It is worth mentioning that, since the heat transfer surface area is fixed by specifying the number of tubes, tube length, and diameter, the recovery ratio is controlled by controlling the feed seawater. While the heat flux inside tubes is fixed, the decreasing of the seawater feed would increase the generated vapor within the tube bundle, that is, increases the process recovery ratio.

2.3. Mesh size and resolution

As shown in Fig. 5, two types of mesh were used in this study; free tetrahedral in the main domain and boundary layer at the walls with adding the corner refinement feature. The used mesh elements are tetrahedral, pyramids, prism, triangular and quadrilateral. Several mesh sizes are considered for the sake of mesh resolution. The studied mesh sizes are (extremely coarse, extra coarse, coarser, coarse, normal and fine).

The pressure drop in the vapor route is calculated at different mesh sizes as shown in Fig. 6. The pressure drop reaches constant at 3,000,000 elements (normal mesh size) and the curve becomes more flattened at 11,000,000 (fine mesh); however it is time consuming. Compromise between time and acceptable resolution, therefore, the predefined normal mesh size is selected in this study where the total number of elements are 3,016,686 while the element quality of ≈ 0.8 and minimum element quality is ≈1.52 × 10^{-6}. The minimum element size has been selected to accurately model the minimum dispersed vapor particle size around the tubes. In addition, the solver convergence termination criteria set at 10^{-5}.

2.4. CFD model verification

MED pilot plant of 24 m^3/d with three effects is considered as case study. The detailed design of the pilot plant is carried out using process design program (VDS) [22]. The evaporator heat transfer area and dimension are calculated accordingly using VDS to be used as fixed domain for CFD simulation. Using the data of Table 1, the 2D CFD program calculate the amount of generated vapor, the average temperature of the generated vapor and exit brine temperature as shown in Figs. 7(a) and (b). As shown in Table 2, there is a good agreement between the CFD model and the VDS simulation program.

The CFD model for two-phase flow has been validated for predicting the pressure drop in the tube bundle using published numerical correlation which presented the appendix

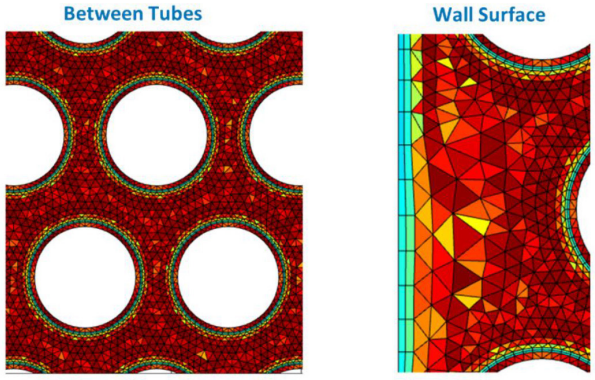

Fig. 5. Types of the mesh.

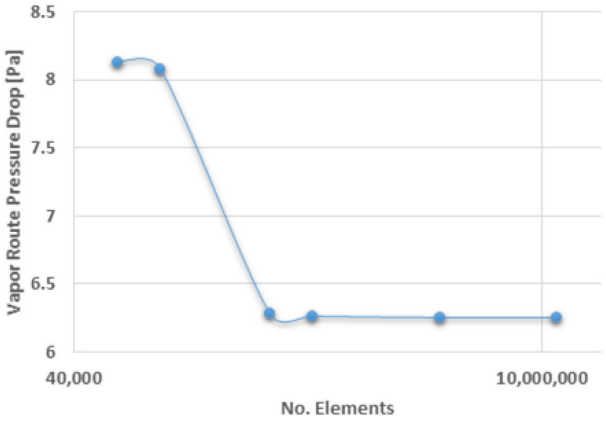

Fig. 6. Pressure drop with variation of the mesh elements.

for the detailed Eqs. (1)–(11) [33]. The CFD numerical model is based on Euler-Euler physics, where the homogeneous void fraction is a function of the recovery ratio, liquid and vapor physical properties and each phase velocity. Fig. 7(c) shows comparison between the two phase CFD model and numerical equation of pressure drop in the tube bundle at different process recovery ratio. The CFD result shows an acceptable agreement with the empirical equation with practical range of the MED process recovery ratio of 20%–40%.

Fig. 7(d) shows the pressure drop in the demister and comparison between the CFD model and the empirical equation based on real experiments from a manufacturer (appendix and Eqs. (12)–(17)) [34]. There is a good agreement between the CFD model and the manufacture equation.

3. Results and discussions

The developed CFD simulation determined the outlet boundary conditions at the side of the evaporator tube bundle and used as input boundary conditions (pressure, velocity, temperature) to the demister. Since the vapor velocity profile is not uniform at the evaporator bundle sides, it massively affects the uniformity at the inlet demister and the vapor box before approaching the next evaporator. Therefore, the calculated local vapor velocity profile at the evaporator exit side which extracted from CFD simulation is applied as an inlet boundary to the demister. As shown in Figs. 8(a) and (b), the local velocity is low at the bottom of the tube bundle while

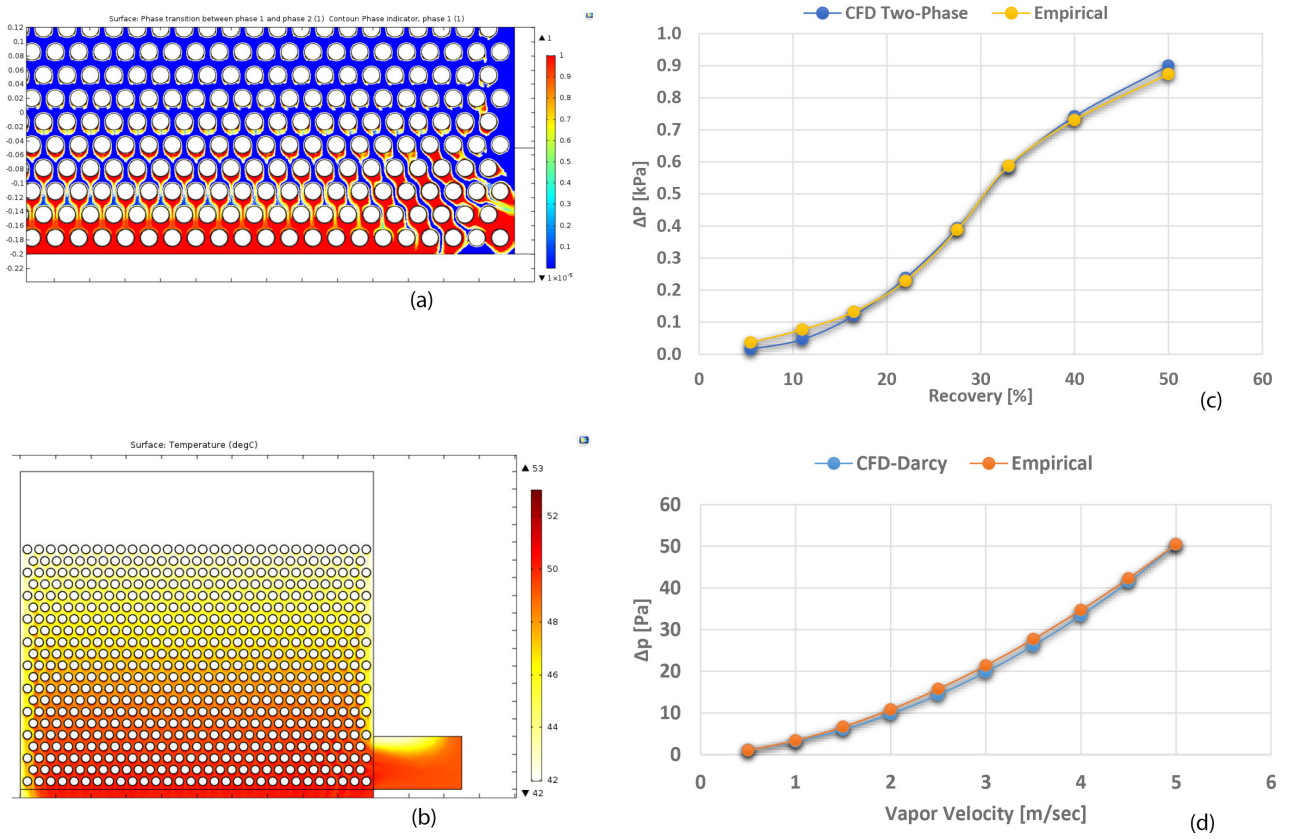

Fig. 7. (a) Vapor volume fraction contour for the effect at 52°C. (b) Temperature contour for the evaporator at 52°C. (c) Verification of two phase CFD model. (d) Verification of the CFD model for demister.

Table 2
Comparison between CFD simulation and process flow program (VDS)

Parameter	VDS program	CFD model
Generated vapor temperature, °C	50.0	50.13
Brine temperature, °C	50.65	50.63
Mass of generated vapor, m^3/h	0.36	0.34

it increases up to 40 m/s at the height of the demister bed. The average velocity at the exit of the tube bundle is 5 m/s as shown in Fig. 8(a).

The CFD model predicts the velocity distribution in 3D domain (demister and vapor box only) as shown in Figs. 9(a) and (b) for both MED-LT and MED-CT configurations, respectively. The vapor velocity magnitude is in the range of 3–9 m/s. However, the vapor vector has to change direction while moving out from the demister to reach the next tube sheet of the next effect. This change in the direction would generate un-even vapor distribution while approaching the next tube bundle. The vapor flow uniformity is determined by calculating the standard deviation between the local vapor velocity and the average velocity at the entrance of the tubes. The tube sheet is divided into four equal sections A, B, C, and D as shown in Figs. 10(a) and (b). Average velocity per each section is calculated and then the standard deviation between the zone velocity and the average velocity. Low

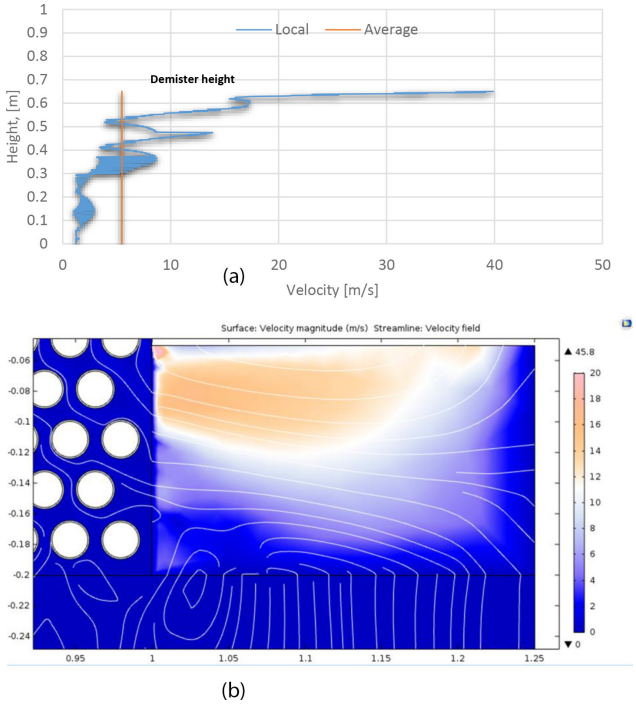

Fig. 8. (a) Local velocity profile at the exit of the tube bundle and before approach demister. (b) CFD velocity profile at the exit of the tube bundle and before approach demister.

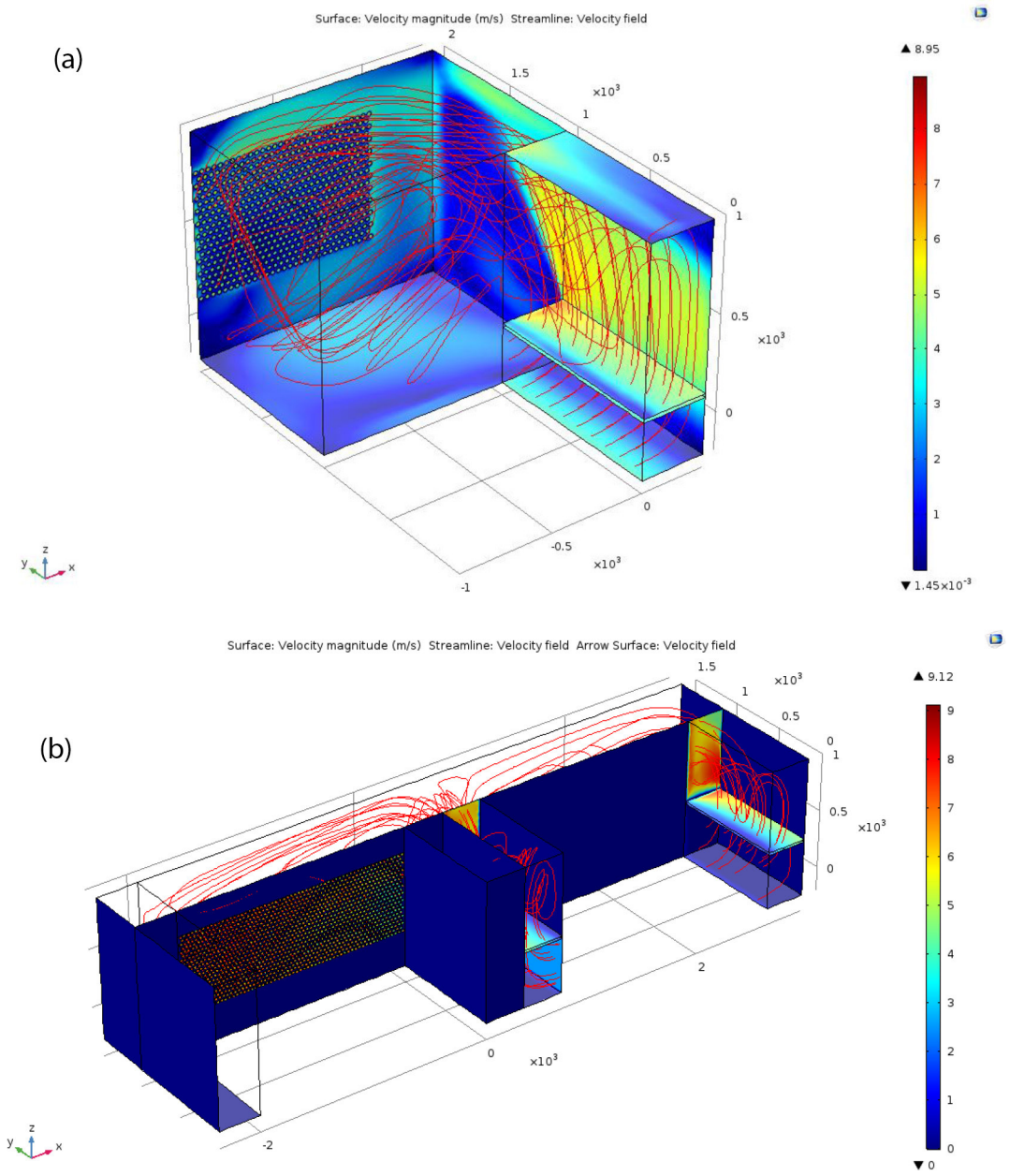

Fig. 9. (a) Velocity magnitude and streamline for MED-LT configuration. (b) Velocity magnitude and streamline for MED-CT configuration.

standard deviation indicates better uniform vapor velocity. As shown in Figs. 10(a) and (b), both configurations show uneven velocity distribution on the tube sheet.

Fig. 11(a) shows the vapor velocity distribution across the tube sheet sections under variable vapor box lengths in the MED-LT evaporator. The average approaching velocity at the tube sheet is calculated as 5 m/s. The local vapor velocity distribution in the section A and B is higher than the average velocity (5 m/s), however, the local vapor velocity distribution in sections C and D is lower than the average velocity (5 m/s). This is because of the sections A and B are close to the vapor outlet from the previous effect as shown in Fig. 3. Nevertheless, the deviation between the section local velocities (A, B, C, and D) and the average velocity decreases as long as the vapor box length increases. This is because of at longer vapor box, the opportunity for better distribution and regain even distribution is higher than shortest vapor box.

Fig. 11(b) shows the velocity distribution per section at different vapor box lengths in MED-CT configuration. The approaching vapor velocity at sections A and B has a negative deviation (i.e., lower than the average vapor velocity of the entire tube sheet), while the vapor velocity at sections C and D has a positive deviation (i.e., higher than the average vapor velocity of the entire tube sheet). This is mainly because of the vapor discharged from the left-side demister is mixed with the vapor discharged from the right-side demister at the vicinity of section A and B. vapor. The potential of creation an eddy flows consequently, push the major part of the vapor

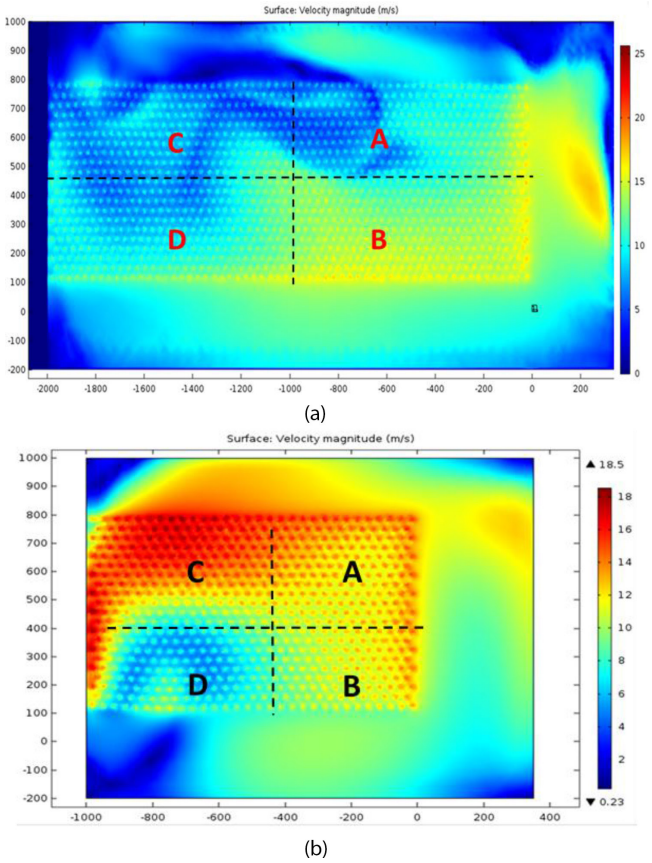

Fig. 10. Vapor velocity profile approaching the tube sheet of the (a) MED-CT configuration and (b) MED-LT configuration.

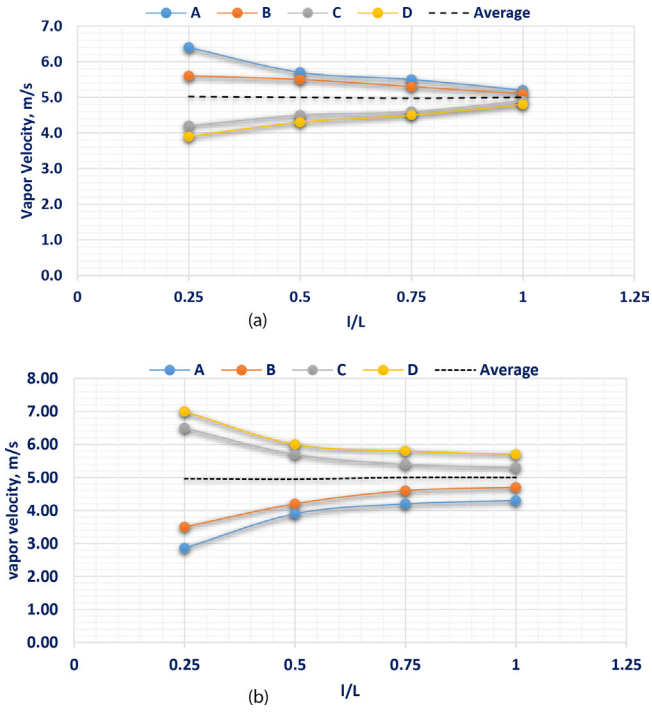

Fig. 11. Distribution of the approaching velocity on the four zones (a) MED-LT and (b) MED-CT.

to the section D and C. Also, in this configuration, the deviation between the section local velocities (A, B, C, and D) and the average velocity decreases when the vapor box length increases. This is because of at longer vapor box, the opportunity for better distribution and regain even distribution is higher than shortest vapor box.

Fig. 12 shows the standard deviation of the vapor velocity distribution for MED-LT and MED-CT evaporators at different vapor box length. The higher standard deviation (less uniformity) is calculated at vapor box length ratio of 0.25, while the vapor velocity distribution among tubes gets uniform at vapor box equal to the tube length (length ratio = 1). Fig. 13 shows that the MED-LT configuration creates a better and uniform vapor flow at all vapor box lengths compared with the MED-CT.

Fig. 13 shows a comparison between the vapor uniformity of the MED-LT and the MED-CT at different values of process recovery ratio. The CFD simulation results show that standard deviation of the vapor distribution in the MED-CT is three times of the MED-LT configuration which implies some tubes will be admitted by amount of vapor higher than the designed, and accordingly will become overheated. Also, while seawater falling on the overheated surface, the scale deposition will be formed, which significantly affects the heat transfer process. On the other hand, for the tubes are under estimated amount of admitted vapor, the insufficient heat is released to generate vapor which affecting the evaporator performance.

The pressure drop occurs within the tube bundle, demister and the vapor box due to friction, separation and sudden

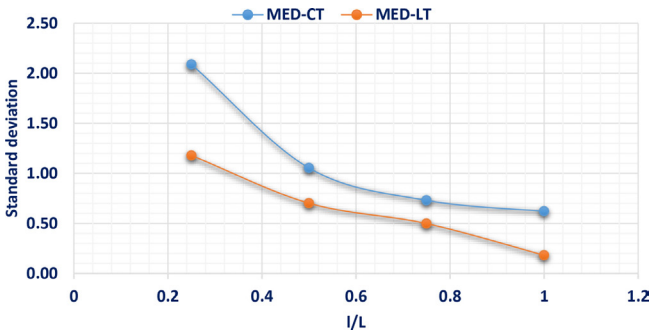

Fig. 12. Velocity standard deviation for both MED-LT and MED-CT configuration.

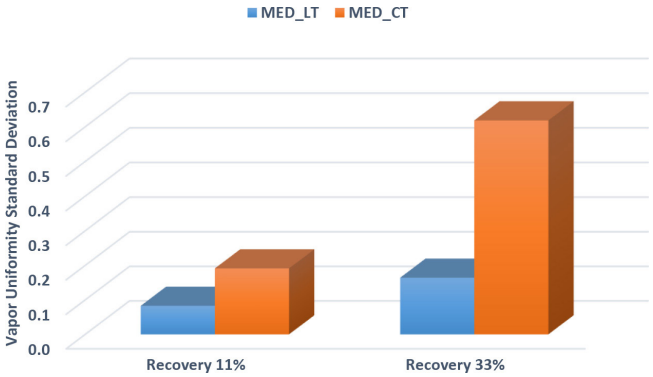

Fig. 13. Effect of recovery on vapor flow uniformity.

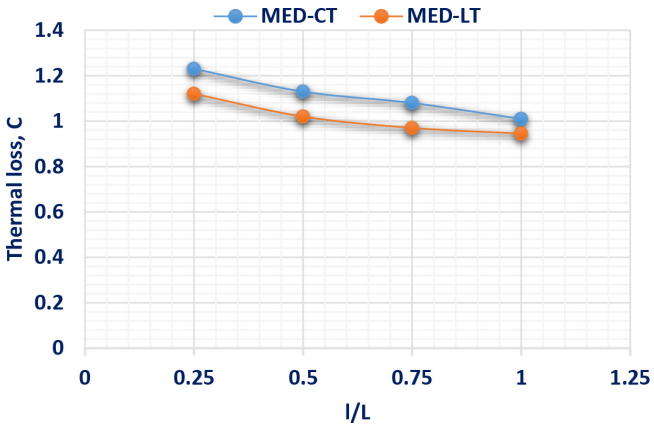

Fig. 14. MED-CT total thermal losses at 33% recovery.

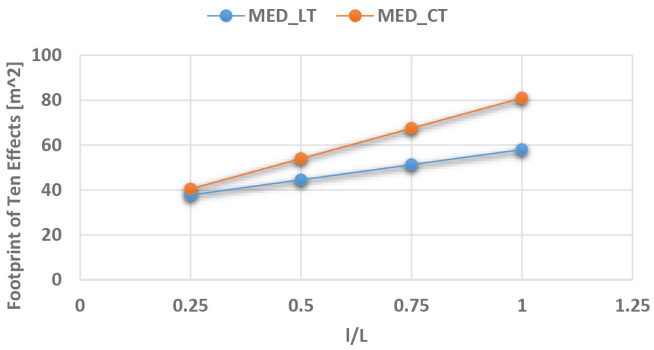

Fig. 15. MED-LT and MED-CT footprint of 10 effects.

change in the flow path, which is expressed by temperature loss or thermal losses. The temperature loss either increases the required heat transfer area (CAPEX increase) or for fixed heat transfer area, the thermal efficiency of the evaporator would decrease. The pressure drop is not only affected by the falling film pattern either columns or droplet but also affected by the friction of crossing vapor over tubes. In fact, as the vapor route becomes longer, the thermal losses get higher (e.g., high-capacity MED). The vapor route resistance would be also affected by the tube orientation, as shown in Fig. 14.

The CFD simulation enables to calculate the total thermal losses encountered in the tube bundle, demister and the vapor box for both MED-LT and MED-CT configurations at different vapor length is shown in Fig. 14. The variation of the vapor box length has slight influence on the thermal losses. This indicates that the thermal loss of the tube bundle is more dominant compared with the losses encountered in the vapor box. Fig. 14 concluded that the thermal losses of the MED-LT is slightly lower than that of the MED-CT because of the layout of the MED-LT create a uniform flow without flow mix and eddy flow which consider a source of pressure drop and consequently thermal loss.

Table 3 shows the thermal losses share at 11% recovery ratio for MED-LT and MED-CT configuration, respectively. The thermal losses include the evaporator tube bundle, demister and vapor box losses. For both configurations, the bundle losses represent 58%, while the demister and vapor box losses are 35% and 7%, respectively. On the other hand,

Table 3
Breakdown of thermal losses

Recovery (%)	Item	MED_LT	MED_CT
11	Evaporator bundle	58.04%	58.27%
	Demister	34.97%	35.10%
	Vapor box	6.99%	6.63%
33	Evaporator bundle	88.03%	88.51%
	Demister	4.29%	4.31%
	Vapor box	7.68%	7.18%

at higher process recovery ratio of 33%, the bundle losses represent 89% of the total thermal losses. This is because of the higher amount of vapor generated at fixed feed seawater, which lead to increasing the vapor velocity around tubes and accordingly increasing the friction losses. Moreover, the vapor box losses at higher vapor velocity are 8% while the demister loss is only 4%. It can be concluded that the evaporator tube bundle is the major part of the total thermal losses. Therefore, it is worthy to exert further efforts to optimize the MED evaporator tube bundle to minimize the cost for MED process.

The footprint is the space area which is occupied by the evaporator. Footprint is important where there is a limitation of the available spaces. Nevertheless, the lower footprint indicates compact evaporator design. Fig .15 shows the footprint of 10 effects of MED-LT and MED-CT evaporators. The footprint increases as the vapor box length increases. The footprint of the MED-CT is 25% higher than the MED-LT configuration, because of the MED-CT needs double number of vapor box of that required for the same number of effects of the MED-LT layout.

4. Conclusion

CFD simulation of the vapor route for the long tube (MED-LT) and the cross tube (MED-CT) configurations were performed to determine thermal losses (tube bundle, demister, and vapor box) and to determine the vapor uniformity in the vapor box. The CFD simulation results show that the standard deviation of the vapor distribution in the MED-CT is three times the MED-LT configuration which implies less vapor uniformity at the next tube sheet. This also indicates that practical and technical challenges would encounter for the MED-CT configuration. This is because some tubes will be admitted by amount of vapor higher than the designed, and accordingly will become overheated. Also, while seawater falling on the overheated surface, the scale deposition will be formed, which significantly affecting the heat transfer process. On the other hand, for the tubes are under estimated amount of admitted vapor, the insufficient heat is released to generate vapor which affecting the evaporator performance.

Analysis of thermal losses show that the tube bundle loss represents 90% of the total losses at 33% process recovery ratio while the rest is encountered in the demister and vapor box. This explains why there is a slight difference of thermal loss between both configurations. Because the thermal losses in the tube bundle have the same value in both configurations. This indicates that the minimization thermal losses in tube bundle are more effective and recommended to focus in

the future work. For the same number of effects, the footprint of the MED-LT configuration is 25% lower than that of the MED-CT configuration. This is because of the MED-CT needs double number of vapor box of that required for the MED-LT configuration.

References

[1] IDA Desalination, Yearbook, 2016–2017.
[2] A. Mabrouk, H. Fath, Technoeconomic study of a novel integrated thermal MSF- MED desalination technology, Desalination, 371 (2015) 115–125.
[3] J. Mitrovic, Preventing formation of dry patches in seawater falling film evaporators, Desal. Wat. Treat., 29 (2011) 149–157.
[4] M.W. Shahzad, A. Myat, W.G. Chun. K.C. Ng, Bubble-assisted film evaporation correlation for saline water at sub-atmospheric pressures in horizontal-tube evaporator, Appl. Therm. Eng., 50 (2013) 670–676.
[5] A.S. Nafey, M. Abdelkader, A. Abdelmotalip, A.A. Mabrouk, Enhancement of solar still productivity using floating perforated black plate. Energy Convers. Manage., 43 (2002) 576–586.
[6] G. Ribatski, A.M. Jacobi, Falling film evaporation on horizontal tubes-a critical review, Int. J. Refrig., 28 (2005) 635–653.
[7] M. Alhaj, A. Mabrouk, S. Al-Ghamdi, Energy efficient multi-effect distillation powered by a solar linear Fresnel collector, Energy Convers. Manage., 171 (2018) 576–586.
[8] K. Thu, Y. Kim, G. Amy, W. Chun, K. Ng, A hybrid Multi-effect distillation and adsorption cycle, Appl. Energy, 104 (2013) 810–821.
[9] M. Shahzad, K. Ng, K. Thu, B. Saha, W. Chun, Multi effect desalination and adsorption desalination (MEDAD): a hybrid desalination method, Appl. Therm. Eng., 72 (2014) 289–297.
[10] M. Shahzad, K. Thu, Y. Kim, K. Ng, An experimental investigation on MEDAD hybrid desalination cycle, Appl. Energy, 148 (2015) 273–281.
[11] M. Shahzad, M. Burhan, H. Son, S. Oh, K. Ng, Desalination processes evaluation at common platform: a universal performance ratio (UPR) method, Appl. Therm. Eng., 134 (2018) 62–67.
[12] K. Ng, M. Shahzad, H. Son, O. Hamed, An Exergy Approach to efficiency evaluation of desalination, Appl. Phys. Lett., 110 (2017) 184101.
[13] A.A. Mabrouk, A.S. Nafey, H. Fath, Steam, electricity and water costs evaluation of power-desalination co-generation plants, Desal. Wat. Treat., 22 (2010) 56–64.
[14] J.J. Lorenz, D. Yung, E.N. Ganic, Vapor/liquid interaction and entrainment in falling film evaporators, J. Heat Transfer, 77 (1980) 69–73.
[15] B.J. Newton, S.A. Moeykens, M.B. Pate, Effects of surface enhancement film feed-supply rate, and bundle geometry on spray evaporation heat transfer performance, ASHRAE Trans., 101 (1995) 408–419.
[16] J.E. Kelly, S.A. Moeykens, M.B. Pate, Spray evaporation heat transfer performance of R123 in tube bundles, ASHRAE Trans., 102 (1996) 259–272.
[17] A. Mabrouk, K. Bourouni, H. Abdulrahim, M. Darwish, A. Sharif, Impacts of tube bundle arrangement and feed flow pattern on the scale formation in large capacity MED desalination plants, Desalination, 357 (2015) 275–285.
[18] H.T. El-Dessouky, H.M. Ettouney, Single effect thermal vapor compression desalination process: thermal analysis, J. Heat Transfer, 20 (1999) 52–68.
[19] J.C. Han, L.S. Fletcher, Falling film evaporation and boiling in circumferential and axial grooves on horizontal tubes, Ind. Eng. Chem. Process Des. Dev., 24 (1985) 570–575.
[20] T.A. Adib, B. Heyd, J. Vasseur, Experimental results and modeling of boiling heat transfer coefficients in falling film evaporator usable for evaporator design, Chem. Eng. Process., 48 (2009) 961–968.
[21] K.R. Chun, R.A. Seban, Heat transfer to evaporating liquid films, Trans. ASME J. Heat Trans., 93C (1971) 391–396.
[22] A.S. Nafey, H.S. Fath, A.A. Mabrouk, A new visual package for design and simulation of desalination processes, Desalination, 194 (2006) 281–296, 423.
[23] A.S. Nafey, H.S. Fath, A.A. Mabrouk, Thermoeconomic investigation of multi effect evaporation (MEE) and hybrid multi effect evaporation-multi stage flash (MEE-MSF) systems, Desalination, 201 (2006) 241–254.
[24] A.N.A. Mabrouk, Techno-economic analysis of tube bundle orientation for high capacity brine recycle MSF desalination plants, Desalination, 320 (2013) 24–32
[25] A.N.A. Mabrouk, Techno-economic analysis of once through long tube MSF process for high capacity desalination plants, Desalination, 317 (2013) 84–94.
[26] A.N.A. Mabrouk, H.E.B.S. Fath, Experimental study of high-performance hybrid NF-MSF desalination pilot test unit driven by renewable energy, Desal. Wat. Treat., 51 (2013) 6895–6904.
[27] M. Mansour, M.A. Qassem, H. Fath, CFD analysis of vapor flow and design improvement in MED evaporation chamber, Desal. Wat. Treat., 56 (2015) 2023–2036.
[28] A.A. Mabrouk, A.S. Nafey, H.E. Fath, Thermoeconomic analysis of some existing desalination processes, Desalination, 205 (2007) 354–373.
[29] M. Ayala, P. Santos, G. Hamester, O. Ayala, Secondary Flow of Liquid-Liquid Two-Phase Fluids in a Pipe Bend, Excerpt from the Proc. 2016 COMSOL Conference in Boston.
[30] N.G. Deen, M. Annal, J.A.M. Kuipers, Multi-scale modeling of dispersed gas–liquid two-phase flow, Chem. Eng. Sci., 59 (2004) 1853–1861.
[31] A.A. Mostafa, H.C. Mongia, On the modeling of turbulent evaporating sprays: Eulerian versus Lagrangian approach, Int. J. Heat Mass Transfer, 30 (1987) 2583–2593.
[32] T.H. Nigim, J.A. Eaton, CFD prediction of flashing processes in a MSF desalination chamber, Desalination, 420 (2017) 258–272.
[33] G. Ribatski, J.R. Thome, Two-phase flow and heat transfer across horizontal tube bundles-a review, Heat Transfer Eng., 28 (2007) 508–524.
[34] http://hanbal.kr/pdf/hanbal.pdf.

Appendix

(i) Pressure drop in two-phase flow

The CFD evaporator bundle two-phase model has been validated with respect to pressure drop against empirical equation based on real experiments [33]. Where, the ratio between the two-phase frictional loss to single phase and accordingly the accounted pressure drop is shown below:

$$\Delta p_{\text{total}} = \Delta p_{\text{static}} + \Delta p_{\text{mom}} + \Delta p_{\text{frict}} \tag{1}$$

where,

$$\Delta p_{\text{static}} = \rho g H \sin\theta \tag{2}$$

For horizontal flow where the θ = 0 and there is no elevation difference, $\Delta p_{\text{static}} = 0$

$$\left[\frac{dp}{dz}\right]_{\text{mom}} = \frac{d\left(\frac{m_{\text{total}}}{\rho}\right)}{dz} \tag{3}$$

For an adiabatic flow, where x is constant, $\left[\frac{dp}{dz}\right]_{\text{mom}} = 0$ Then

$$\Delta p_{\text{total}} = \Delta p_{\text{frict}} = \frac{2G^2 N f_{2\phi}}{\rho} \tag{4}$$

where

$$\frac{f_{2\phi}}{f} = \left(\frac{G}{G_0}\right)^{\frac{-3}{2}} + \left[1 - \left(\frac{G}{G_0}\right)^{\frac{-3}{2}}\right](2x-1)^2 \tag{5}$$

$$f = \frac{16}{Re} \tag{6}$$

$$\text{Re} = \frac{GD}{\mu} \tag{7}$$

$$\mu = \mu_l(1-\varepsilon) + \mu_G \varepsilon \tag{8}$$

$$\rho = \rho_l(1-\varepsilon) + \rho_G \varepsilon \tag{9}$$

$$\varepsilon = \frac{1}{1 + \left(\frac{v_G}{v_l}\frac{(1-x)}{x}\frac{\rho_G}{\rho_l}\right)} \tag{10}$$

where G is the mass velocity, [17]

$$G = \frac{m}{\left[(n_c - 1)\varnothing + 1\right]dL} \tag{11}$$

Δp_{total}: Total pressure drop, Pa
Δp_{static}: Static pressure drop, Pa
Δp_{mom}: Momentum pressure drop, Pa
Δp_{frict}: Frictional pressure drop, Pa
H: Vertical height, m
θ: Angle with reference to horizontal, degree
g: Acceleration due to gravity, m/s²
$f_{2\varphi}$: Two-phase pressure drop, dimensionless
f: Single-phase pressure drop, dimensionless
Re: Reynolds number, dimensionless
G_0: Reference mass velocity, 400 kg/m²s
G: Mass velocity, kg/m²s
x: Recovery/vapor quality, fraction
ε: Homogeneous void fraction
N: Number of tube rows
$\frac{v_G}{v_l}$: Velocity ratio or slip ratio (S), dimensionless
m: Mass flow rate, kg/s
n_c: Number of tubes per row
Ø: Tube pitch, m
μ_l: Liquid viscosity, Pa s
μ_G: Vapor viscosity, Pa s
ρ_l: Liquid density, kg/m³
ρ_G: Vapor density, kg/m³
μ: Two-phase viscosity, Pa s
ρ: Two-phase density, kg/m³
D: Outside tube diameter, m

(ii) Pressure drop in the demister

The manufacturer equations [34] along with demister main parameters are shown below: -

$$\Delta p = \frac{f * t * (1-\varepsilon_v) * \rho_v * v_{\max}^2}{D_w} \tag{12}$$

$$f = 5.3\left(\frac{\rho_v * v_{\max}^2 * D_w}{\mu_v}\right)^{-0.32} \tag{13}$$

$$v_{\max} = k\frac{\sqrt{(\rho_l - \rho_v)}}{\rho_v} \tag{14}$$

$$v_{\text{optimum}} = 0.8 v_{\max} \tag{15}$$

where,

t: Demister thickness, 0.15 m
ε_v: Void fraction "porosity", 0.98
D_w: Wire diameter, 0.0003 m
k: Demister coefficient, 0.108
$v_{\max}$: Maximum allowable vapor velocity
v_{optimum}: Optimum operational vapor velocity

The demister is a porous media over a definite thickness where the accounted pressure change is identified as a combination of Darcy's law and the inertial loss term [34] as follows: -

$$\Delta p = t\left(\frac{v * \mu_v}{\alpha} + \frac{C_2 * \rho_v * v^2}{2}\right) \quad (16)$$

$$\alpha = \frac{D_w{}^2 * \varepsilon_v{}^3}{150 * \left(1-\varepsilon_v\right)^2} \quad (17)$$

$$C_2 = \frac{3.5 * \left(1-\varepsilon_v\right)}{D_w{}^2 * \varepsilon_v{}^3} \quad (18)$$

where,

α: Permeability

C_2: Pressure jump coefficient